

Influence of Miura-origami shapes on drag in turbulent flows

By T. Zahtila[†], L. Chan [†], A. Ooi[†], K. Liu, M. Benjamin AND G. Iaccarino

This work uses data from direct numerical simulation (DNS) to examine the drag-reduction potential of different surfaces generated from a Miura-origami basis—folded, creased material structures with no tearing. Miura surfaces span a wide set of possible realizations but presently are deployed to emulate optimized drag-reducing riblets. Flexibility of the Miura fold also permits modified surfaces that transform traditional straight riblets by including an additional streamwise wavelength, i.e., triangular riblets with streamwise waviness. As such, we report the drag-reduction characteristics of a set of Miura surfaces to identify optimal configurations. To build confidence in our findings, code-to-code verification is performed by comparing two flow solvers that perform DNS of a separate, complex, highly skewed Miura-fold roughness topology. Comparing their respective output statistics, a good level of agreement is observed. Returning to the drag-reducing wavy riblets, turbulence quantities are collected to explore modulation of dynamical scales through premultiplied energy spectra. The literature shows that dynamically oscillating walls are able to deplete streaks in the streamwise turbulent fluctuations, but until now the efficacy of the passive analogue had been unknown. Further, alignment of near-wall structures with the wavy surface topology is visualized and quantified to reveal the wall-normal extent to which the wall may affect turbulence. The primary objective of this work establishes the potential for static wavy Miura surfaces to enhance drag reduction as compared to classical straight riblets. Drag decomposition reveals that the role of a thickening viscous region is responsible for the shift in observed performance. This is a first step toward actuated dynamic origami surfaces in a drag-reduction context.

1. Introduction

Origami is the Japanese art of folding paper. A basic feature of origami is that intricate designs can be reversibly achieved by folding along predetermined lines. Origami is used in many engineering problems (Turner et al. 2016), such as in packaging and storage, optics, space, soft robotics (Hawkes et al. 2010), and biomedical devices. The origami fold that is of interest in this project is the Miura fold, which was initially invented for use in space solar panels (Miura 1985), allowing the panels to be condensed to a compact shape for efficient transportation to space. Upon deployment, the structure would fold out into its purposeful form.

A single repeating unit of the Miura fold is illustrated in Figure 1. The crease patterns on the Miura fold consist of parallelograms with side lengths of l_1 and l_2 , and the acute angle of the parallelogram is dictated by γ . For a surface with predetermined l_1 , l_2 , and γ , changing θ determines the so-called crumple of the surface. Although it is not the subject of this work, Miura folds could be exploited for actuated surfaces, e.g., in the presence of an electric field. More broadly, Miura folding a sheet of material increases

[†] Department of Mechanical Engineering, University of Melbourne, Australia

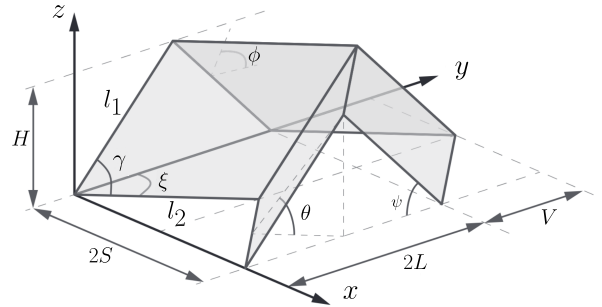


Figure 1: Base unit of the Miura fold, taken from Schenk & Guest (2013).

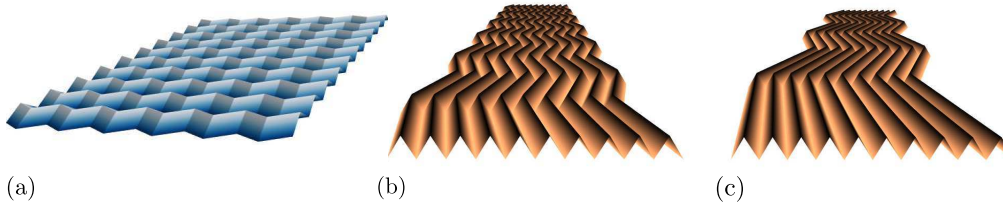


Figure 2: Miura-fold realizations, (a) complex roughness topology used for code-to-code verification and (b,c) two possible riblet modifications, with variation in streamwise wavelength.

the structural rigidity of the overall object. The enhanced mechanical properties of the Miura fold as a metamaterial has been investigated thoroughly (Schenk & Guest 2013). It is important to emphasize that the appeal of Miura origami lies in the wide range of surfaces that can be constructed. Figure 2 shows some of these realizations such as the 3-D roughness topology shown in Figure 2(a), used in the verification studies in this work, alongside two surfaces that modify a straight riblet, shown in Figure 2(b,c), which differ by a factor of two in wavelength λ of the streamwise transform. In this work, the principal geometric variables of interest are the viscous scaled wavelength λ^+ (+ denotes viscous scaling) that transforms the traditional straight riblet, and the associated transform amplitude a . While from a fluid dynamics perspective these are the variables of interest, these surfaces are nonetheless generated from the origami parameters l_1 , l_2 , γ , and θ and constitute realizable surfaces from a Miura fold. Fluid dynamics research into these surfaces has mostly been overlooked despite this being an important subject that requires attention, as these surfaces are well suited for soft-robotics implementations or deployment in amphibious vehicles. In this work, we will consider turbulent flow over the Miura fold and its capability to reduce drag.

Efforts to develop textured surfaces that can passively decrease drag have been ongoing since the early 1980s (Bechert & Bartenwerfer 1989; Walsh 1980). Surfaces such as streamwise aligned riblets are known to decrease drag. The streamwise-aligned grooves of these surfaces reduce skin friction drag by physically restricting the lateral instability in the viscous sublayer (Bechert & Bartenwerfer 1989), which reduces the spanwise turbulence intensity immediately above the riblets (Bechert et al. 1997). This mechanism forces the near-wall vortices (Kline et al. 1967) to exist further from the surface, thus lowering the vertical transfer of streamwise momentum. This drag-reducing mechanism

is well established and is associated with the viscous thickening of the sublayer. Researchers have sought to improve this drag-reducing device; one proposed modification is the use of sinusoidal-like rods (Peet et al. 2008), which were found to introduce cross-flow motions that varied with phase, and better drag reduction was observed when the sinusoidal-like rods were of streamwise wavelength $\lambda_x^+ = 1080$. Those findings pertained to a friction Reynolds number $Re_\tau = 180$ and were obtained via large-eddy simulation of turbulent channel flow and attention restricted to quantification of drag reduction through skin friction drag, but these results are more complicated when pressure drag also forms part of the analysis. A similar DNS work was performed, again at $Re_\tau = 180$, with a primary focus on sinusoidal modification to trapezoidal riblets (Okabayashi 2016), and the optimal wavelength for drag reduction was found to be $\lambda_x^+ = 1131$. Flow over Miura-origami riblets has been investigated at $Re_\tau = 180$ for one streamwise wavelength, $\lambda_x^+ = 565$ (Okabayashi et al. 2018). This study found that, in the plane above the riblet tips, streamwise vortices tilt in the spanwise direction interrupting vortex stretching, improving performance on straight riblets.

More recently, drag reduction has been pursued through an alternative pathway, active surface actuation. Recent experimental work conducted by Marusic et al. (2021) showed that substantial drag reduction of up to 25% is obtained by oscillating walls. For clarification, that experiment entailed vigorously sliding spanwise slats that constituted an energy input. The spanwise oscillation of the wall caused a breakdown of the near-wall structures, thereby reducing the turbulence intensity near the wall. While a substantial drag reduction was obtained, the net energy input of the system must be taken into account, and net energy savings were obtained for higher Reynolds numbers because dynamic oscillation targeting the outer-region large eddies required feasible low-frequency actuation. Accordingly, for most known problems of engineering interest, it will be important to investigate the applicability of Miura origami at higher Reynolds numbers.

In this work, starting from straight, optimally grooved triangular riblets, streamwise variation in the spanwise direction is added to the surface via the Miura fold to investigate whether enhanced drag reduction is obtained. This can be considered an attempt at a passive analogue of the aforementioned oscillating-wall configuration. Future work might exploit the dynamic capability of Miura folds for further improvements. Further, conclusions drawn in this manuscript are only preliminary from an application perspective, as emergence of the outer energy peak in turbulent energy is properly studied when $Re_\tau > 1700$ (Hutchins & Marusic 2007), which is crucial for the drag-reduction pathway reported by Marusic et al. (2021).

2. Methodology

2.1. Code-to-code verification

The spectral elements used in NekRS (Fischer et al. 2021) require a purely hexahedral mesh that may be highly skewed when body-fitted to sharp geometrical features such as surface roughness. Skewed elements affect the convergence of spectral element discretization (Shams & Komen 2018). To code-to-code verify the results obtained from the NekRS simulations, a representative set of calculations is reproduced using NaluCFD (Domino 2015), a generalized unstructured low-Mach solver. NaluCFD has a control-volume finite-element method hybrid discretization (Schneider & Raw 1987), supporting

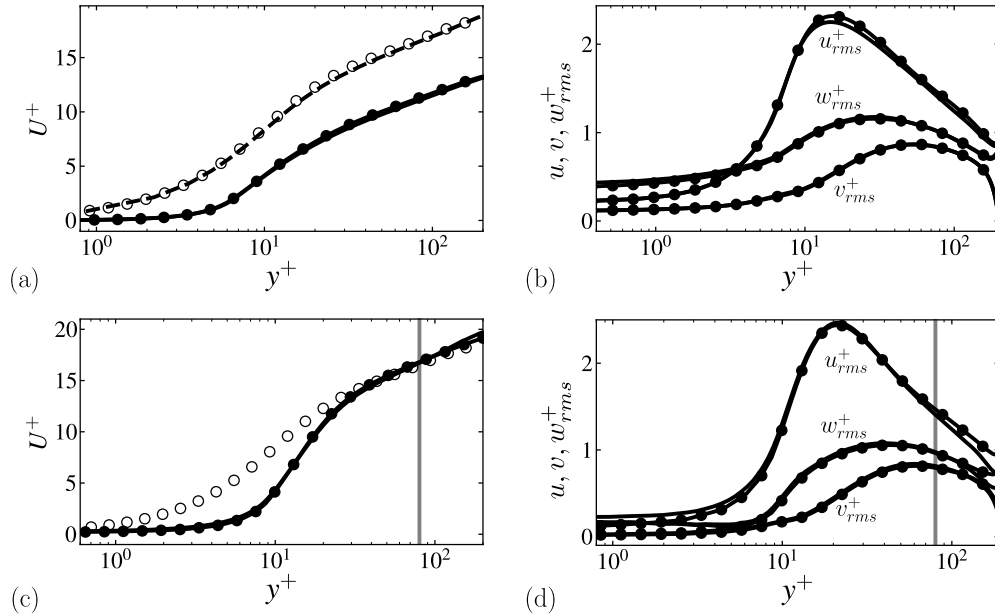


Figure 3: Verification of NaluCFD against NekRS at $Re_\tau = 200$. Verification of complex roughness topology: (a,b) mean streamwise velocity profile and turbulent statistics. Verification of straight riblets case: (c,d) mean streamwise velocity profile and turbulent statistics. Solid lines: NekRS. Filled circles: NaluCFD. Open circles: smooth wall reference data from Moser et al. (1999). Dashed line: smooth wall mean streamwise velocity profile from NekRS. Vertical lines in (c,d) demarcate extent of accurate minimal channel for NekRS output.

both linear and quadratic basis functions for tetrahedral and hexahedral elements, allowing for second- or third-order-accurate simulations (Domino 2018).

Three plane half-channel flows are considered: smooth wall, straight riblets, and a complex Miura-origami roughness surface (see Figure 2(a)). Additionally, smooth wall channel reference data (Moser et al. 1999) are included to build trust in the smooth wall half-channel flow. All comparative simulations are performed at a friction Reynolds number of $Re_\tau = 200$. The NekRS simulation of the straight riblets is carried out with a reduced spanwise domain, i.e., a minimal channel, as established by MacDonald et al. (2017). The NaluCFD simulations with straight riblets were carried out with a linear basis, while the quadratic basis was employed for the complex origami case, as minor differences in the outputted mass flux were observed with only a linear basis. The straight riblets reproduce the geometry considered by Peet et al. (2008), with a riblet spacing $s/\delta = 0.1164$ and a riblet height of $h/\delta = 0.1$. A domain of streamwise size $L_x^+ = 1600$ and spanwise size $L_z^+ = 400$ is considered to accommodate all present near-wall structures, with a resolution for the NaluCFD simulations of $(\Delta_x^+, \Delta_y^+, \Delta_z^+) = (4.6 \times 0.1 \times 2.6)$ in the streamwise, wall-normal (minimum), and spanwise dimensions, respectively. The low-Mach equations are time-integrated using a second-order backward differentiation formula (BDF-2). As with the NekRS calculations, a uniform constant-pressure gradient is added as a nodal source term to the streamwise momentum equation.

The mean streamwise velocities and turbulence intensities for the complex origami

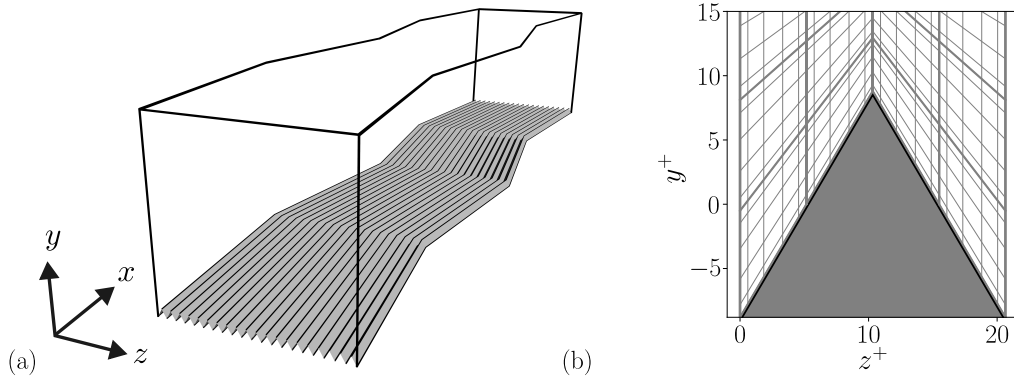


Figure 4: Visualization of (a) the computational triangular half-channel domain employed in this work and (b) a body-fitted Gauss-Lobatto-Legendre spectral element method mesh.

roughness topology and straight riblets cases are shown in Figure 3. The two solutions are in good agreement for the origami case, with less than 1% error for all statistics. Similarly good results are observed for the straight riblets; however, the NekRS profiles degrade in accuracy at $y^+ > 80$, which is a known trade-off for a minimal-span channel (Chung et al. 2015). The smooth wall simulation results are indistinguishable between the two codes.

2.2. Numerical implementation

For the cases in Table 1, DNS was conducted for a turbulent half-channel at friction Reynolds number $Re_\tau = 400$, solving the incompressible Navier-Stokes equations

$$\frac{\partial \mathbf{u}}{\partial t} + \nabla \cdot (\mathbf{u}\mathbf{u}) = -\frac{1}{\rho} \nabla p + \nabla \cdot (\nu \nabla \mathbf{u}) + F_p, \quad (2.1)$$

$$\nabla \cdot \mathbf{u} = 0, \quad (2.2)$$

where F_p is a uniform streamwise forcing constant-pressure gradient, and all primitive variables retain their usual meaning. Visualizations of the computational domain and mesh are provided in Figure 4. The meshing follows the standard Gauss-Lobatto-Legendre (GLL) distribution within spectral elements. The mesh for all cases is composed of 181,400 spectral elements with a polynomial order of five, constituting a total of 39.2M total nodes resulting in GLL grid spacing of $\Delta_x^+ = (4.56, 11.1)$, and, typically for the element adjacent to the wall, $\Delta_y^+ = (0.49, 1.77)$ and $\Delta_z^+ = (0.60, 1.47)$. At the surface, a no-slip boundary condition is applied with symmetry on the top of the half-channel. The remaining sides are periodic faces.

3. Results

The wavelength- and amplitude-varying Miura-origami surfaces that were investigated are outlined in Table 1, where the first four digits of each case ID correspond to the streamwise wavelength λ^+ followed by the amplitude-to-wavelength ratio a/λ . These surfaces are obtained from an origami transform of the near-optimal straight riblet configuration with the viscous-scaled square root of the groove cross-sectional area $l_g^+ = 13$;

Case ID	l_g^+	k^+	λ^+	a/λ	L_x^+	L_z^+	ΔU^+	$L_t u_\tau / \delta$	Symbol
0000_0.00	13.48	17.60	∞	0	3264	412.9	-0.540	63.8	— —
0270_0.03	13.48	17.59	271	0.03	3258	413.5	-0.560	43.9	●
0540_0.03	13.48	17.59	542	0.03	3257	413.5	-0.608	66.9	■
0540_0.06	13.50	17.56	539	0.06	3239	415.3	-0.573	33.4	■
1080_0.03	13.48	17.59	1085	0.03	3257	413.5	-0.578	102.8	★
1080_0.06	13.50	17.56	1080	0.06	3239	415.3	-0.519	31.5	★
1080_0.12	13.57	17.45	1054	0.12	3164	422.5	-0.300	21.1	★
1620_0.03	13.48	17.59	1628	0.03	3257	413.5	-0.629	63.1	✱
1620_0.06	13.50	17.56	1619	0.06	3239	415.3	-0.522	32.5	✱
straight_misa	13.48	17.60	∞	0	3264	412.9	-0.490	33.2	●
origami_misa	13.48	17.59	1628	0.03	3257	413.5	-0.567	39.6	●

Table 1: Summary of the conducted simulations. l_g^+ is the riblet cross-sectional area, k^+ is the riblet height, λ^+ is the viscous-scaled wavelength and a/λ is the amplitude-to-wavelength ratio of a triangular wave associated with the origami streamwise variation. L_x^+ and L_z^+ are the streamwise and spanwise domain lengths in viscous scaled + units, and $L_t u_\tau / \delta$ is the statistical sampling interval. Repeated symbols are contextualized in individual figures to refer to a specific case.

the remaining parameters, e.g., k^+ , are interconnected and also vary slightly. Further, two supplementary flow misalignment cases representatively compare straight and origami riblets. Note that variation in the statistical sampling interval $L_t u_\tau / \delta$ is due to case 1080_0.03 forming an initial exploratory case, longer sampling was considered for cases with $a/\lambda = 0.03$, as these were drag reducing.

3.1. Drag reduction

Drag reduction can be related to a smooth wall at a matched friction Reynolds number Re_τ by $DR \equiv 1 - C_D / C_{D,smooth}$. The drag coefficient is $C_D = \tau_w / (0.5\rho U_b^2)$, where

$$\tau_w \equiv \frac{\int_S (-pn_x + \mu \mathbf{n} \cdot \nabla \mathbf{u}) dS}{A_t}, \quad (3.1)$$

where A_t is plan area as opposed to the wetted area A_w allowing for comparisons between surfaces, the first term is the pressure drag and the second is the viscous stress. However, as we are utilizing computationally efficient minimal channels, in lieu of measuring U_b we evaluate the viscous-scaled mean velocity profile at a matched height in the logarithmic layer to determine the roughness function, $\Delta U^+ = U_{smooth}^+ - U^+$. We use the superscript + to denote quantities scaled with the viscous scales, i.e., $U^+ = U/U_\tau$ ($U_\tau = \sqrt{\tau_w/\rho}$ is the friction velocity and τ_w is the wall shear stress). Computing ΔU^+ at a matched height follows the established approach of Endrikat et al. (2021), so $DR \propto -\Delta U^+$. The streamwise mean velocity profiles for the optimal amplitude-to-wavelength ratio are shown in Figure 5, accompanied by the charted roughness function ΔU^+ for the simulations in Table 1. The straight riblets, case 0000_0.00, have a roughness function value of $\Delta U^+ = -0.540$ and are within the data scatter of triangular-shaped riblets summarized by Endrikat et al. (2021). In that work, the reported sampling time interval corresponds to a computational domain with a unit plan area that is ~ 2.5 times smaller than in our simulations, and so the present sampling interval can be regarded as similar. Further, the convergence criterion we employ is collapse of the total shear stress budget onto the expected linear profile. The drag reduction shows a maximum 16% improvement on

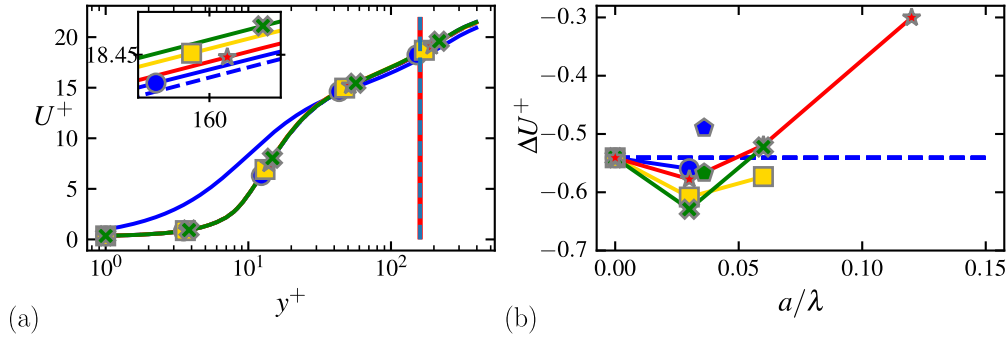


Figure 5: Comparison of straight and origami riblets: (a) mean streamwise velocity profiles comparing a selection of the conducted simulations, smooth wall, straight riblets, and origami riblets from Table 1 with amplitude-to-wavelength ratio $a/\lambda = 0.03$, and (b) corresponding roughness function ΔU^+ as a function of a/λ . Misaligned cases are slightly offset from true $a/\lambda = 0.03$ for visual contrast.

the drag reduction obtained from classical straight riblets for $a/\lambda = 0.03$ for a wavelength $\lambda^+ = 1620$. All wavelengths investigated show a deterioration in drag reduction when a/λ is increased beyond the optimal ratio $a/\lambda = 0.03$, which can be attributed to increasing pressure drag, which in turn is found to grow rapidly with increasing wave amplitude. Our results suggest the prospect of origami-based optimization of straight-riblets—and, indeed, the more general inclusion of a streamwise mode—is limited to a small amplitude-to-wavelength ratio a/λ . The roughness function ΔU^+ suggested a non-linear dependency on the streamwise wavelength λ^+ , which requires further attention in subsequent work. Connecting the present work to existing zig-zag riblet findings at $Re_\tau = 180$ (Okabayashi et al. 2018), the zig-zag simulations report a different relationship between ΔU^+ and a/λ . Two regimes emerge: First, with increasing a/λ , the bulk velocity drops, but for $a/\lambda > 0.07$, the benefits of large viscous drag reduction outweigh the pressure drag penalty, with a maximum reported drag-reduction enhancement of 13%. The discrepancy between that study and the present findings can be attributed to a different triangular riblet starting shape and a possible Reynolds number dependency. We now aim to unpack the presently reported ΔU^+ quantities.

3.2. Turbulence modification

For brevity in turbulence description, we report on the turbulent spectra by which the turbulent state is well characterized. In this section, we report the 1-D and 2-D spectra of the streamwise velocity u , to highlight the contribution of streamwise λ_x and spanwise λ_z length scales to the eddy energy distribution. The 2-D spectrum is a further decomposition of the 1-D spectrum into wavenumbers for the spanwise direction z , and its utility is a closer look at the energy distribution at a given wall-normal location. Mathematically, the energy in the spectra can be integrated to return the signal variance, i.e., turbulent fluctuations, and premultiplication preserves a desirable plotting property, that of equal plotted areas corresponding to equal energy contribution

$$\int_0^\infty \phi_{uu} dk_x = \int_0^\infty k_x \phi_{uu} d(\log k_x) = \overline{u^2}, \quad (3.2)$$

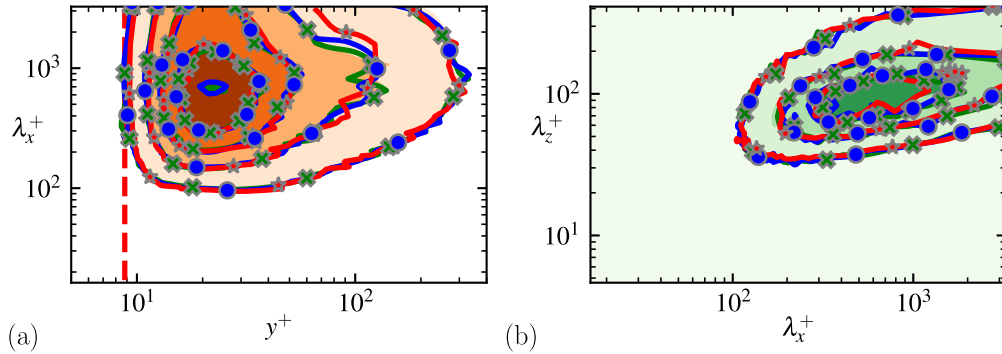


Figure 6: For the optimal amplitude of $a/\lambda = 0.03$, the plotted cases are, 0270_0.03 and 1620_0.03, and for the non-optimal high amplitude $a/\lambda = 0.12$, the case plotted is 1080_0.12, (a) 1-D premultiplied energy spectra, contour levels beginning at 0.3 with increments of 0.4, and (b) 2-D spectra taken at $y^+ = 15$. Contour levels begin at 0.2 with increments of 0.3. The dashed red vertical line indicates the location of riblet tips.

and the energy in the 2-D spectrum is similarly defined as

$$\phi_{uu}(k_x, k_z, y) = k_x k_z \langle \hat{u} \hat{u}^* \rangle. \quad (3.3)$$

The 1-D premultiplied energy spectrum for straight riblets is characterized by a shift in wavelength space for the dominant energy-containing eddies, from $\lambda_x^+ = 1000$ to 800, also shifting away from the wall from $y^+ = 15$ to $y^+ = 25$. This indicates breakup of the larger structures in addition to spanwise motion constraints arising from the riblet geometry. In Figure 6(a) we plot filled contours of the the 1-D spectra for the straight riblets, and then overlay the same energy contours from select origami cases. We include contours from 1080_0.12 as an exploratory case. Although its ΔU^+ profile shows poor drag reduction because the spanwise amplitude is too high, this case is included to test for potential modification to energy-containing structures. The turbulent energy scales are not further affected by the presence of origami variations in the straight riblets. We corroborate this finding by plotting the 2-D spectra taken at $y^+ = 15$ in Figure 6(b), and we still observe the same structure of turbulent scales. The persistence of turbulent scales when the surface undergoes transformation of a streamwise mode distinguishes the considered surfaces from the mechanisms present in dynamic oscillating walls and requires further interrogation.

To substantiate this finding, we decompose the flow field into its fluctuating components (u', v') and perform classical quadrant analysis (Wallace et al. 1972). However, in this case, we focus on streamwise-spanwise orientation of structures, so contours of the wall-fleeing $Q2$ ($u' < 0, v' > 0$) events were extracted. The results from the high-amplitude 1080_0.12 case showed, as expected a strong correlation between the $Q2$ structures and wall orientation, for structures directly on the plane above the riblet tips (see Figure 7(a)). However, this correlation quickly disappeared even a few viscous units further away from the wall, and the mean streamwise-spanwise orientation of the structure was independent of the wall phase underneath. A similar statistic was computed in Miura-fold riblets by Okabayashi et al. (2018), who found that the conditionally sampled spanwise velocity in the plane above the riblet tips showed an induced spanwise velocity that varied with riblet phase. We also note that this phase correlation decays

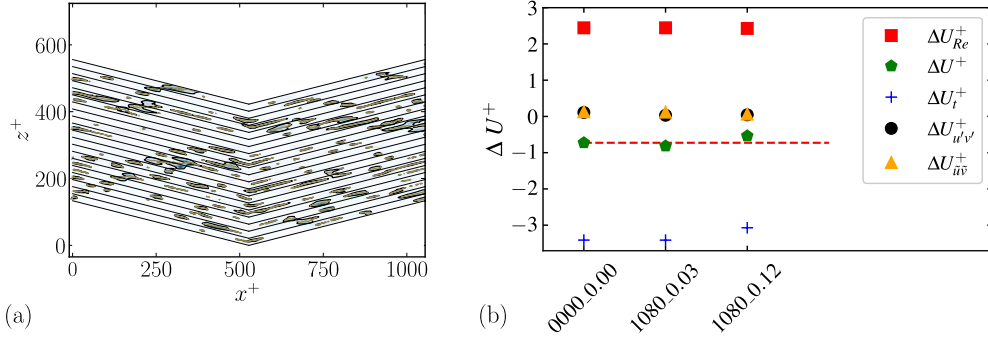


Figure 7: (a) Alignment of ejection structures ($Q2$ events) with the underneath origami surface sketched for case 1080_0.12. Plane taken at $y^+ = 10$, i.e, marginally above the riblet tip. Spines of the threshold isocontours are drawn in gold and the statistics of these spines are then post-processed. (b) Drag decomposition for three reference cases from Table 1.

just a few viscous units further away from the wall. This motivates two considerations: (i) Passive mechanisms have a restricted ability to affect structures that reside in the buffer layer, and (ii) the dynamical significance of the near-wall streaks requires further attention. However, the particulars of the phase correlation in the near-wall region may be Reynolds number dependent, and when $Re_\tau > 2000$ is considered, the near-wall region is influenced by large-scale footprints and small-scale modulation (Marusic et al. 2010), shaping the future workflow required to demonstrate generality of these present findings.

3.3. Drag decomposition

Decomposition of skin friction profiles is an existing technique whereby the Reynolds averaged Navier-Stokes equation is integrated to split the contributions from laminar, turbulent, and inhomogeneous/unsteady stresses (Fukagata et al. 2002). This concept has been extended to rough walls, where the mean momentum balance is equated between a smooth and a rough wall (MacDonald et al. 2016) to produce the roughness function decomposition,

$$\begin{aligned}
 \Delta U^+ = & \underbrace{U_{smooth}^+(y_t^+) - U^+(y_t^+)}_{\Delta U_t^+} + \underbrace{\int_{y_t^+}^{y_c^+} \frac{\delta'_{smooth} - y^+}{\delta_{smooth}^+} - \frac{\delta' - y^+}{\delta^+} dy^+}_{\Delta U_{Re}^+} \\
 & + \underbrace{\int_{y_t^+}^{y_c^+} \overline{u'v'}_{smooth} - \overline{u'v'}^+ dy^+}_{\Delta U_{u'v'}^+} + \underbrace{\int_{y_t^+}^{y_c^+} -\tilde{u}\tilde{v}^+ dy^+}_{\Delta U_{\tilde{u}\tilde{v}}^+}, \quad (3.4)
 \end{aligned}$$

where t is the riblet tip height, δ_{smooth} is the smooth wall boundary layer thickness (or the channel height), and δ' is the effective boundary layer thickness, which is measured from the virtual origin (riblet crest) to the half-channel height. In a minimal-span channel, $y_c = 0.4L_z$ (Chung et al. 2015). Note that $\delta_{smooth} = \delta'_{smooth} = \delta$. For the streamwise velocity u , $\tilde{\cdot}$ denotes coherent velocity fluctuation and $'$ denotes total fluctuation. The contributions of these terms were computed for three cases: (i) a straight riblet 0000_0.00,

(ii) 1080_0.03, and (iii) 1080_0.12, which corresponds to a reference comparison with enhanced and degrading drag reduction for origami configurations, plotted in Figure 7(b). To perform this analysis, the virtual origin is taken to be the riblet tip, hence the augmented overall ΔU^+ values on a smooth wall. The change in the dispersive ($\Delta U_{\bar{u}\bar{v}}^+$) and friction Reynolds number (ΔU_{Re}^+) terms did not show appreciable difference between the considered surfaces, but the mean velocity profile at the riblet tip (ΔU_t^+) and Reynolds stress ($\Delta U_{u'v'}^+$) accounted for the change in the overall roughness function. For the improved drag-reduction case, 1080_0.03, the tip velocity ΔU_t^+ was higher than the straight riblet 0000_0.00, suggesting a thickened viscous sublayer, but this was no longer the case for 1080_0.12.

3.4. Flow misalignment

Two additional cases, `straight_misa` and `origami_misa`, are run with oncoming flow at a 10° misalignment with the streamwise direction of the channel, with details reported in Table 1, in order to gauge the robustness of drag reduction in the origami surface. This is achieved by modifying the pressure forcing to include a component in the spanwise direction. Flow misalignment is an important consideration because in nature, the mean flow will rarely be aligned with the surface as is set up in laboratory or numerical experiments. Actually, in both the straight and origami riblets, a similar performance degradation occurred (-9.3% versus -9.8%), but nevertheless these surfaces remained drag reducing, and the misaligned origami surface still performed better than the straight riblets with aligned flows.

4. Conclusions

A systematic investigation of origami surfaces was performed as a potential pathway to improvement of riblets. Starting with the near-optimal straight riblet configuration with the viscous-scaled square root of the groove cross-sectional area $l_g^+ = 13$, transformations that introduce a triangular wave to the surface yielded a 16% drag-reduction performance increase when compared with conventional straight riblets. With increasing amplitude, rapid performance degradation occurs, so the potential benefit is limited. However, this work did not consider Miura surfaces derived from straight riblets with non-optimal groove cross-sectional area, e.g., $l_g^+ = 50$, and this physics remains unknown. Therefore, we do not form general conclusions. Importantly, from the point of view of turbulence considerations, the basic science of riblets—that of constrained vortices that shift away from the wall—remains present, and passive waviness did not modify the energy in the turbulent scales. This topic was reviewed with both 1-D and 2-D premultiplied energy spectra. However, a thickening of the viscous sublayer was identified as responsible for the shift in the mean velocity profile, which affected drag-reduction performance.

Acknowledgments

The authors acknowledge use of computational resources from the Yellowstone cluster awarded by the National Science Foundation to CTR, as well as computing time on the Quartz supercomputer at Livermore Computing.

REFERENCES

- BECHERT, D. W. & BARTENWERFER, M. 1989 The viscous flow on surfaces with longitudinal ribs. *J. Fluid Mech.* **206**, 105–129.

- BECHERT, D. W., BRUSE, M., VAN DER HAGE, W., VAN DER HOEVEN, J. G. & HOPPE, G. 1997 Experiments on drag-reducing surfaces and their optimization with an adjustable geometry. *J. Fluid Mech.* **338**, 59–87.
- CHUNG, D., CHAN, L., MACDONALD, M., HUTCHINS, N. & OOI, A. 2015 A fast direct numerical simulation method for characterising hydraulic roughness. *J. Fluid Mech.* **773**, 418–431.
- DOMINO, S. P. 2015 Sierra low Mach module: Nalu theory manual 1.0. *SAND2015-3107W*, Sandia National Laboratories.
- DOMINO, S. P. 2018 Design-order, non-conformal low-Mach fluid algorithms using a hybrid CVFEM/DG approach. *J. Comput. Phys.* **359**, 331–351.
- ENDRIKAT, S., MODESTI, D., GARCÍA-MAYORAL, R., HUTCHINS, N. & CHUNG, D. 2021 Influence of riblet shapes on the occurrence of Kelvin–Helmholtz rollers. *J. Fluid Mech.* **913**, A37.
- FISCHER, P., KERKEMEIER, S., MIN, M., LAN, Y. H., PHILLIPS, M., RATHNAYAKE, T., MERZARI, E., TOMBOULIDES, A., KARAKUS, A. & CHALMERS, N. 2021 NekRS, a GPU-accelerated spectral element Navier–Stokes solver. *Parallel. Comput.* **114**, 102982.
- FUKAGATA, K., IWAMOTO, K. & KASAGI, N. 2002 Contribution of reynolds stress distribution to the skin friction in wall-bounded flows. *Phys. Fluids* **14**, L73–L76.
- HAWKES, E., AN, B., BENBERNOU, N. M., TANAKA, H., KIM, S., DEMAINE, E. D., RUS, D. & WOOD, R. J. 2010 Programmable matter by folding. *Natl. Acad. Sci. USA* **107**, 12441–12445.
- HUTCHINS, N. & MARUSIC, I. 2007 Large-scale influences in near-wall turbulence. *Philos. R. Soc. A* **365**, 647–664.
- KLINE, S. J., REYNOLDS, W. C., SCHRAUB, F. A. & RUNSTADLER, P. W. 1967 The structure of turbulent boundary layers. *J. Fluid Mech.* **30**, 741–773.
- MACDONALD, M., CHAN, L., CHUNG, D., HUTCHINS, N. & OOI, A. 2016 Turbulent flow over transitionally rough surfaces with varying roughness densities. *J. Fluid Mech.* **804**, 130–161.
- MACDONALD, M., CHUNG, D., HUTCHINS, N., CHAN, L., OOI, A. & GARCÁ-MAYORAL, R. 2017 The minimal-span channel for rough-wall turbulent flows. *J. Fluid Mech.* **816**, 542.
- MARUSIC, I., CHANDRAN, D., ROUHI, A., FU, M. K., WINE, D., HOLLOWAY, B., CHUNG, D. & SMITS, A. J. 2021 An energy-efficient pathway to turbulent drag reduction. *Nat. Commun.* **12**, 5805.
- MARUSIC, I., MATHIS, R. & HUTCHINS, N. 2010 Predictive model for wall-bounded turbulent flow. *Science* **329**, 193–196.
- MIURA, K. 1985 Method of packaging and deployment of large membranes in space. *Inst. Space Astronaut. Sci. Rep.* **618**, 1–9.
- MOSER, R., KIM, J. & MANSOUR, N. 1999 Direct numerical simulation of turbulent channel flow up to $Re_\tau=590$. *Phys. Fluids* **11**, 943–945.
- OKABAYASHI, K. 2016 Direct numerical simulation for modification of sinusoidal riblets. *J. Fluid Sci. Technol.* **11**, JFST0015.
- OKABAYASHI, K., HIRAI, K., TAKEUCHI, S. & KAJISHIMA, T. 2018 Direct numerical simulation of turbulent flow above zigzag riblets. *AIP Adv.* **8**, 105227.
- PEET, Y., SAGAUT, P. & CHARRON, Y. 2008 Turbulent drag reduction using sinusoidal riblets with triangular cross-section. *AIAA Paper* 2008-3745.

- SCHENK, M. & GUEST, S. D. 2013 Geometry of Miura-folded metamaterials. *P. Natl. Acad. Sci. USA* **110**, 3276–3281.
- SCHNEIDER, G. E. & RAW, M. J. 1987 Control volume finite-element method for heat transfer and fluid flow using collocated variables—1. Computational procedure. *Numer. Heat Transf. A* **11**, 363–390.
- SHAMS, A. & KOMEN, E. M. J. 2018 Towards a direct numerical simulation of a simplified pressurized thermal shock. *Flow Turbul. Combust.* **101**, 627–651.
- TURNER, N., GOODWINE, B. & SEN, M. 2016 A review of origami applications in mechanical engineering. *Proc. Inst. Mech. Eng. C* **230**, 2345–2362.
- WALLACE, J. M., ECKELMANN, H. & BRODKEY, R. S. 1972 The wall region in turbulent shear flow. *J. Fluid Mech.* **54**, 39–48.
- WALSH, M. J. 1980 Drag characteristics of V-groove and transverse curvature riblets. In *Viscous Drag Reduction*, pp. 168–184. AIAA.